Swell Transformation across the Continental Shelf. Part I: Attenuation and Directional Broadening

FABRICE ARDHUIN

Centre Militaire d'Océanographie, Service Hydrographique et Océanographique de la Marine, Brest, France

W. C. O'REILLY, T. H. C. HERBERS, AND P. F. JESSEN

Department of Oceanography, Naval Postgraduate School, Monterey, California

(Manuscript received 23 July 2002, in final form 27 December 2002)

ABSTRACT

Extensive wave measurements were collected on the North Carolina–Virginia continental shelf in the autumn of 1999. Comparisons of observations and spectral refraction computations reveal strong cross-shelf decay of energetic remotely generated swell with, for one particular event, a maximum reduction in wave energy of 93% near the Virginia coastline, where the shelf is widest. These dramatic energy losses were observed in light-wind conditions when dissipation in the surface boundary layer caused by wave breaking (whitecaps) was weak and wave propagation directions were onshore with little directional spreading. These observations suggest that strong dissipation of wave energy takes place in the bottom boundary layer. The inferred dissipation is weaker for smaller-amplitude swells. For the three swell events described here, observations are reproduced well by numerical model hindcasts using a parameterization of wave friction over a movable sandy bed. Directional spectra that are narrow off the shelf are observed to broaden significantly as waves propagate over the inner shelf, although refraction theory predicts a narrowing. This broadening generally agrees with predictions of Bragg scattering of random waves by the irregular seafloor topography.

1. Introduction

The evolution of waves in shallow water is the result of many processes including atmospheric forcing, the nonlinear dynamics of the wave motion, and the influence of bottom topography and surficial sediments. Winds directly force the high-frequency (''wind sea'') part of the wave spectrum, actively generating waves with phase speeds slower than the wind speed, and a large fraction of this energy input is immediately lost through wave breaking (whitecaps). The low-frequency (''swell'') part, with larger phase speeds, can be influenced indirectly by local winds through nonlinear wave–wave interactions. In intermediate to shallow water (shallower than the surface wavelength), the influence of the bottom becomes important and manifests itself through wave refraction, topographic scattering, and dissipation of wave energy by bottom friction. As local winds often dominate the wave climate of such shallow locations, such as the North Sea, investigations of the spectral energy balance of waves are faced with the difficult task of separating all these processes (e.g., Bouws and Komen 1983; Weber 1988; Johnson and Kofoed-Hansen 2000). However, outside the surf zone and in the absence of a wind sea or strong currents, the steepness of swell is generally too small to induce wave breaking, and the propagation distances across continental shelves are typically too short for significant nonlinear transfers of energy across the spectrum. Hence swell transformation across the shelf is controlled primarily by wave–bottom interactions and is thus more tractable for analysis. Nevertheless, few studies of swell evolution have been presented, owing primarily to a lack of detailed field measurements (e.g., Hasselmann et al. 1973; Young and Gorman 1995; Herbers et al. 2000; Ardhuin et al. 2001). Here we present new observations from the Shoaling Waves Experiment (SHOWEX) that took place in 1999 on the U.S. East Coast offshore of the North Carolina Outer Banks. Detailed measurements of the evolution of directional wave spectra across this sandy shelf were recorded over a three-month period, including numerous swell events with a wide range of peak frequencies, amplitudes, and directions. This new dataset is used here, in combination with a spectral wave model, to evaluate the effects of wave–bottom interaction processes.

The paper is organized as follows. A brief review of wave–bottom interactions processes over fine to medium sand is given in section 2. Wave and weather con-

Corresponding author address: Dr. Fabrice Ardhuin, EPSHOM/CMO, 13 rue du Chatellier, Brest, Cedex 29609, France.
E-mail: ardhuin@shom.fr

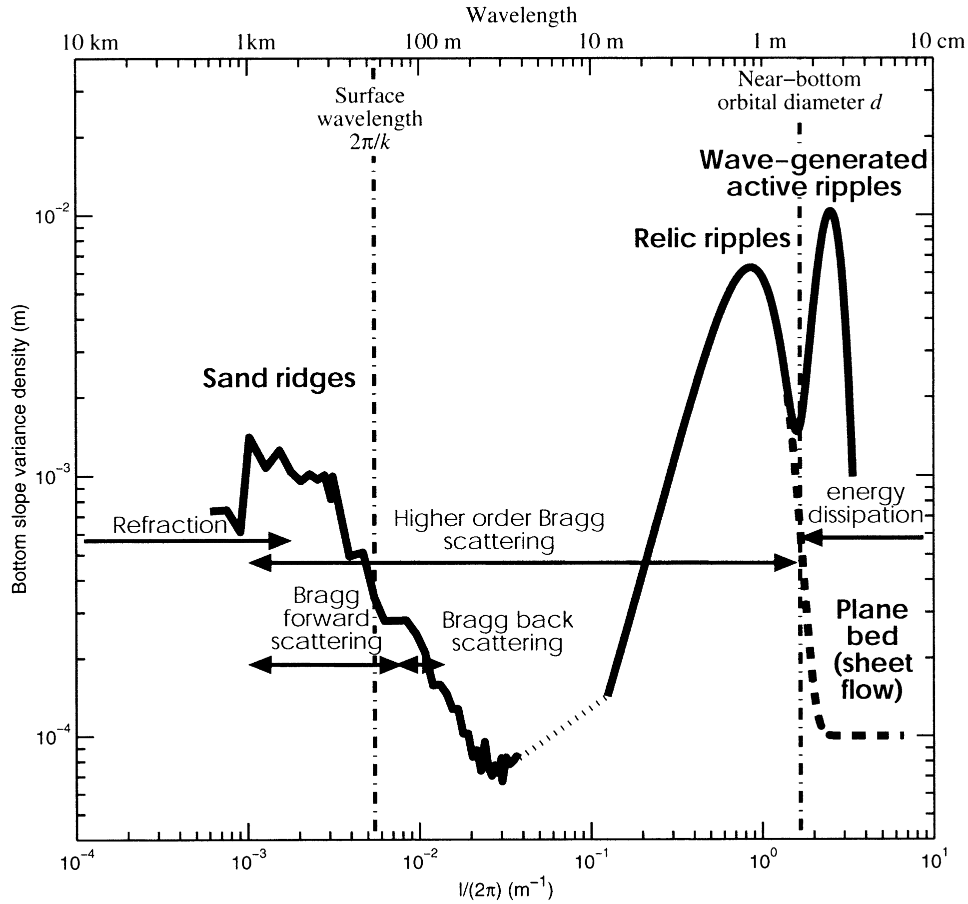

FIG. 1. Wave–sandy bottom interactions, for different topography scales (the x-axis coordinate $2\pi/l$ is the reciprocal bottom wavelength). The thick curve is a typical bottom slope spectrum for the North Carolina shelf derived from bathymetry surveys for bottom wavelengths larger than 40 m. At small scales ($2\pi/l <$ 10 m) the bottom topography depends on the wave conditions typically varying from a rough rippled bed in moderate swell conditions (solid curve), to a smooth plane bed for very large swells (dashed curve).

ditions and observations during SHOWEX are presented in section 3. An implementation of the CREST wave model (Ardhuin et al. 2001) is described in section 4, and is used in section 5 to examine the effects of various physical processes in three swell events. Conclusions are given in section 6. In Ardhuin et al. (2003, hereinafter Part II) SHOWEX data are used, together with observations from the earlier DUCK94 experiment in the same region, to evaluate different parameterizations of the spectral energy balance of swell on the continental shelf.

2. Wave–bottom interaction processes over a sandy bottom

Swell is modified by a wide range of bottom topography and roughness scales (Fig. 1). The well-known refraction and shoaling of waves by large-scale (>1 km) topography (e.g., Mei 1989) can cause dramatic variations in nearshore wave conditions that are predicted accurately by linear propagation models (e.g., Munk and Traylor 1947; O'Reilly and Guza 1993). Less understood are the effects of intermediate scales that can be described with wave–bottom Bragg scattering theory (Hasselmann 1966; Long 1973; Ardhuin and Herbers 2002) and small-scale roughness elements (0.1–10 m) that enhance wave energy dissipation (Zhukovets 1963).

Hasselmann (1966) proposed a statistical theory for the Bragg scattering of random waves by irregular topography, assuming spatially homogeneous conditions (i.e., uniform surface wave and bottom elevation spectra). At the lowest order, two wave components with the same radian frequency ω but different wavenumber vectors $\mathbf{k}$ and $\mathbf{k}'$ exchange energy in a resonant triad interaction with the bottom component that has the difference wavenumber $\mathbf{l} = \mathbf{k} - \mathbf{k}'$. Depending on the bottom wavenumber $\mathbf{l}$ surface waves may be scattered forward, broadening the directional spectrum (Ardhuin and Herbers 2002), or backward, attenuating the incident wave field (Long 1973). Hasselmann's theory was recently extended to heterogeneous conditions (with a correction of the wave–bottom coupling coefficient) and included in the form of a source term S_{Bragg} in a spectral wave model (Ardhuin and Herbers 2002). Application to the North Carolina continental shelf showed negligible backscattering, but strong forward scattering on the inner shelf that nearly doubled the directional spread of wave energy at the peak frequency, in qualitative agreement with observations. Directional observations were limited to one site on the inner shelf and thus precluded a quantitative assessment of the theory.

At smaller seabed scales, ripples strongly influence bottom friction induced by the near-bed wave orbital motion over noncohesive sandy sediments. Neglecting mean currents, the bottom boundary layer can be classified in three regimes, based on the ratio of friction and buoyant forces acting on a sand grain, and represented by the Shields number ψ (e.g., Nielsen 1981). For small values of ψ, the bottom morphology does not change, thus retaining the history of past wave events and biological activity. In this ''relic roughness'' regime with weak orbital wave motion and turbulence, wave energy dissipation is minimal. As ψ increases past a threshold value ψ_c (typically 0.05 for well-sorted quartz sand), the wave flow intermittently moves surficial sediments that organize into ripple fields (e.g., Nielsen 1981; Traykovski et al. 1999). Turbulent vortices are shed by the orbital flow at the crests of these ''active ripples,'' enhancing the bed hydrodynamic roughness experienced by the waves and causing a sharp increase in the dissipation of wave energy. Widespread presence of ripples with wavelengths in the range 0.5–3 m was observed in repeated sidescan sonar surveys of the North Carolina shelf, performed during SHOWEX (Ardhuin et al. 2002a). Changes in the geometry of these ripples between surveys were shown to correspond fairly well to wave orbital diameters and propagation directions in preceding wave events when the ripples were likely formed. Whereas the development of ripples is relatively well understood, little is known about how a rippled bed adapts to changing wave conditions or restores to a flat bed. With increasing forcing conditions ($\psi > \psi_c$) ripples are progressively eroded, until they are completely flattened for $\psi > 10\psi_c$ (Li and Amos 1999), when a layer of sediments (the ''sheet flow'') moves back and forth with the water column. In this sheet flow regime the dissipation of wave energy is relatively weaker (Ardhuin et al. 2001).

3. The SHOWEX deployment

a. Instruments and data analysis

Extensive wave measurements were collected from September to December 1999 across the wide shelf of the Mid-Atlantic Bight, in the region between Cape Hatteras and the entrance to the Chesapeake Bay (Fig. 2). A transect of six surface-following Datawell Directional Waverider buoys (X1–X6) was deployed extending east from the U.S. Army Corps of Engineers Field Research Facility (FRF) at Duck, North Carolina, to the shelf break. A coherent array of five bottom pressure recorders was collocated with inner shelf buoy X2 to provide high-resolution directional wave spectra. In the present study we also use data from other directional wave-measuring instruments routinely deployed in the region. Near the shelf break, the National Data Buoy Center (NDBC) operates a 3-m discus pitch-and-roll buoy (44014), in 49-m depth. Close to shore, a coherent array of bottom pressure sensors in 8-m depth (8M) and a Datawell Directional Waverider buoy in 15-m depth [WR(FRF)] are both maintained by the FRF. Additionally, infrared laser wave gauges on the Diamond Shoals (DSLN7) and Chesapeake Lighthouse (CHLV2) C-MAN stations, operated by NDBC, provided estimates of wave frequency spectra at shallow-water sites away from the main instrument transect. The instrument locations are indicated in Fig. 2 and their basic characteristics are summarized in Table 1.

The dataset includes both directional (buoys and coherent pressure arrays) and nondirectional (laser gauges) wave measurements. Although some instruments are ideally equivalent (e.g., Datawell and NDBC directional buoys), different sampling frequencies, record lengths, and response characteristics introduce some variations in quality. The model–data comparisons presented below are generally restricted to bulk parameters that can be estimated reliably from the short records of routine wave measurement systems. The significant wave height, $H_s = 4(E)^{1/2}$, with E the surface elevation variance in the frequency range 0.03–0.15 Hz, was estimated at all instrumented sites. At directional buoy sites the mean direction θ_p and directional spread $\sigma_{\theta,p}$, both evaluated at the spectral peak frequency f_p, were determined from auto- and cross-spectra of the buoy displacements (e.g., Long 1980) using the standard approximations of these parameters in terms of the lowest-order Fourier moments of the directional spectrum a_1 and b_1,

$$[a_1(f),\, b_1(f)] = \int_0^{2\pi} (\cos\theta,\, \sin\theta)E(f,\, \theta)\, d\theta/E(f). \quad (1)$$

At the high-resolution 8M array, estimates of full frequency–directional spectrum $E(f,\, \theta)$ (Long and Atmadja 1994) were used to evaluate $a_1(f)$ and $b_1(f)$, after excluding the small contribution of offshore propagation waves. In order to initialize the model at the offshore boundary, $E(f,\, \theta)$ estimates were obtained from the farthest offshore buoys X6 and 44014 using the Maximum Entropy Method (Lygre and Krogstad 1986). All spectra and directional parameters were interpolated on a common frequency grid, also shared by the numerical model CREST in the hindcasts described below, and reduced to energy-weighted averages over 1-h intervals.

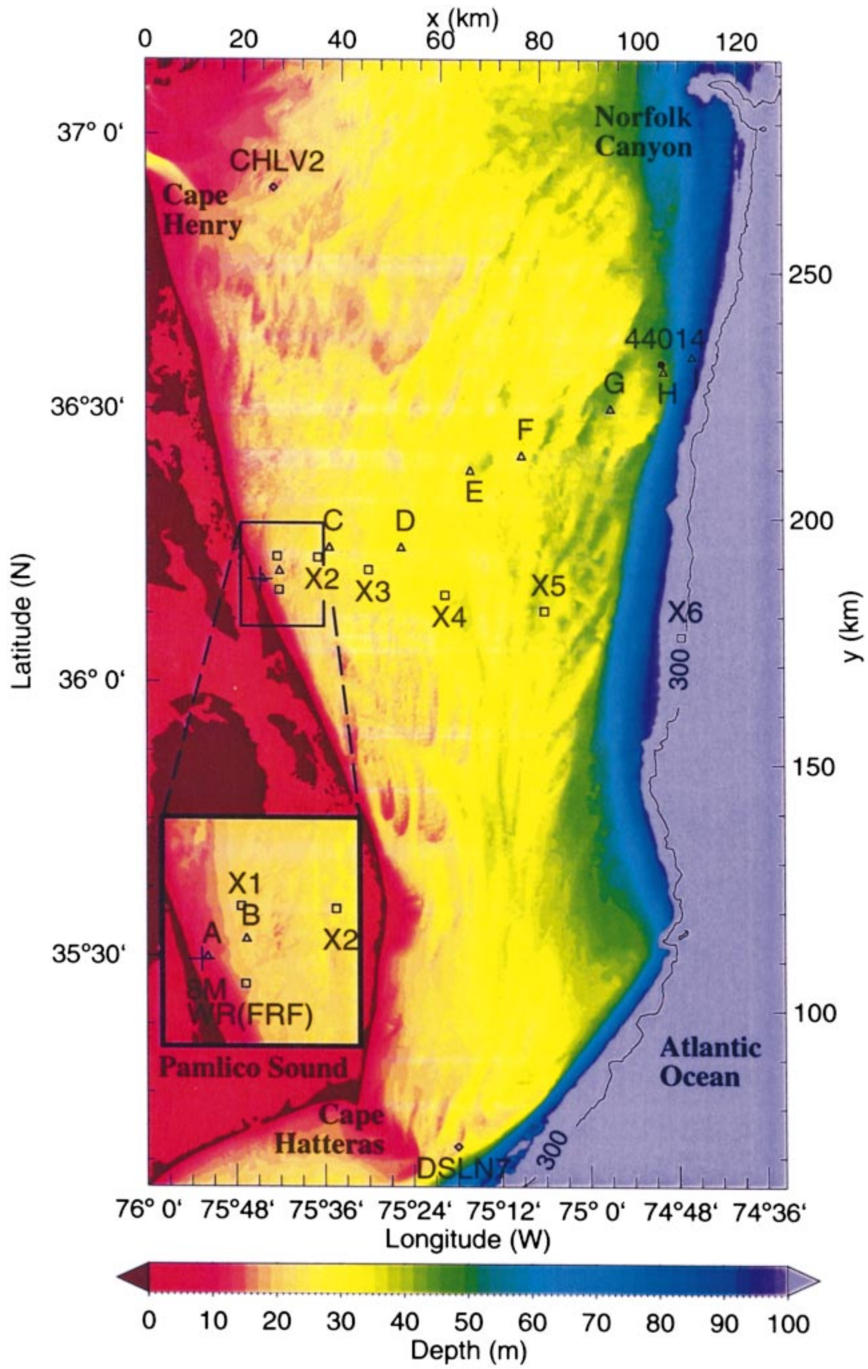

FIG. 2. Bathymetry and instrument locations during DUCK94 and SHOWEX (see text and Table 1 for instrument descriptions).

b. Wave conditions

The dominant wave events in the Mid-Atlantic Bight are generally the result of tropical storms and hurricanes in the summer–early autumn, which follow a curved path to the northwest along the coast, and nor'easter storms in late autumn–winter, which develop over North America and move offshore into the North Atlantic. SHOWEX took place in the middle of the very active 1999 hurricane season. Deployments at sea were delayed by a few days owing to category-4 Hurricane Dennis (30 August–5 September), and within two days after the instrument installation was completed, category-4 Hurricane Floyd made landfall south of Cape Hatteras. The maximum offshore significant wave heights observed during Floyd varied from 6.8 m at

TABLE 1. Wave-measuring instruments during SHOWEX.

Name	Type	Water depth (m)	Directional	Operated by
8M	Pressure array	8.0	Yes	FRF
WR (FRF)	Buoy	17.0	Yes	FRF
44014	Buoy	49	Yes	NDBC
CHLV2	Laser gauge	15	No	NDBC
DSLN7	Laser gauge	18	No	NDBC
X1	Buoy	21	Yes	NPS
X2	Buoy	24	Yes	NPS
X2A	Pressure array	24	Yes	NPS
X3	Buoy	26	Yes	NPS
X4	Buoy	33	Yes	NPS
X5	Buoy	39	Yes	NPS
X6	Buoy	193	Yes	NPS

44014, 9.0 m at X6, to 12.5 m farther south at NDBC buoy 41004 (located at 34°30′N, off Charleston, South Carolina, not shown) with a peak frequency of 0.11 Hz. A maximum sustained wind speed $U_{19.5} = 34$ m s^{-1} was recorded at the end of the FRF pier. Immediately after Floyd left the region, a new hurricane, Gert, reached category 4, but remained far offshore, sending large-amplitude swell over the shelf (f_p about 0.07 Hz, H_s up to 3.0 m at X6, 3.4 m at 44014). These three major hurricanes were followed by two weaker hurricanes. The eye of Hurricane Irene crossed the Florida Peninsula from the Gulf of Mexico into the Atlantic and passed 100 km offshore of Cape Hatteras, while Jose followed a track similar to that of Gert (Fig. 3). SHOWEX was also marked by several nor’easter storms, with a particularly severe event on 1 December.

4. Numerical model implementation

a. The CREST wave model

CREST is a hybrid Eulerian–Lagrangian spectral wave model that uses finite frequency–direction bands and an unstructured geographical grid (Ardhuin et al. 2001). The spectral energy balance equation is solved in its Lagrangian form,

$$\frac{dE(\mathbf{k})}{dt} = S_{\mathrm{Bragg}}(\mathbf{k}) + S_{\mathrm{fric}}(\mathbf{k}), \tag{2}$$

where the left-hand side is the rate of change of the wavenumber spectral energy density $E(\mathbf{k})$ following a wave component along its ray trajectory. Equation (2) is solved along precomputed ray trajectories, from the model domain boundary to each point of the geographical grid. A first-order Euler scheme with a fixed 10-min time step is used, and the spectral density is av-

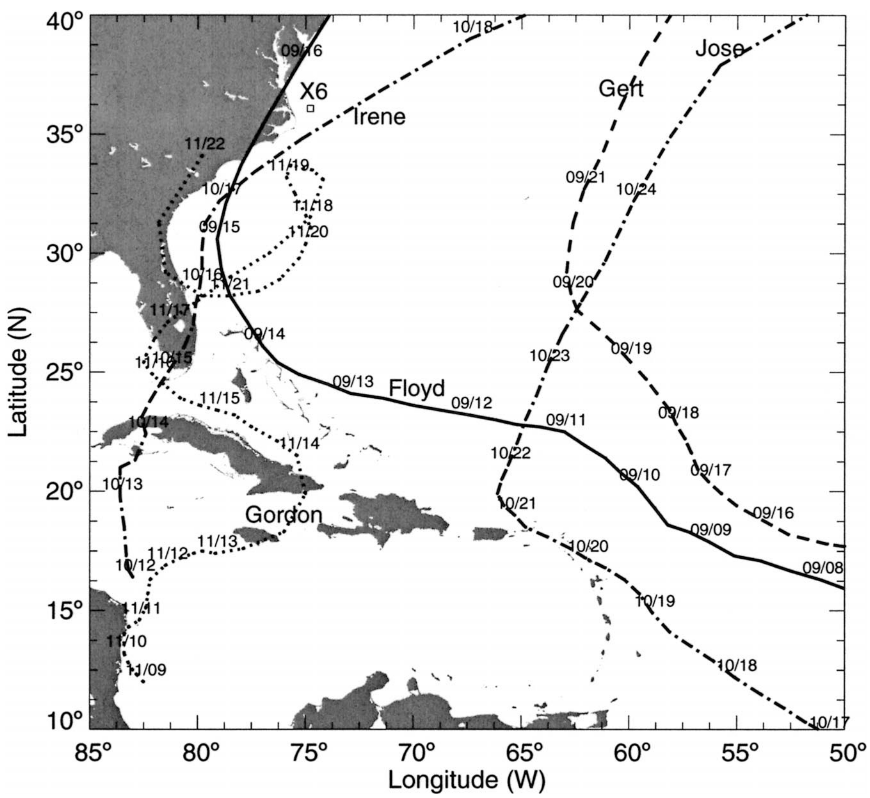

FIG. 3. Tracks of North Atlantic Hurricanes Gordon (during DUCK94), Floyd, Gert, Irene, and Jose (all four during SHOWEX). The dates indicate the daily position of the eye of the storm, at 1200 EST, after reaching the tropical depression stage.

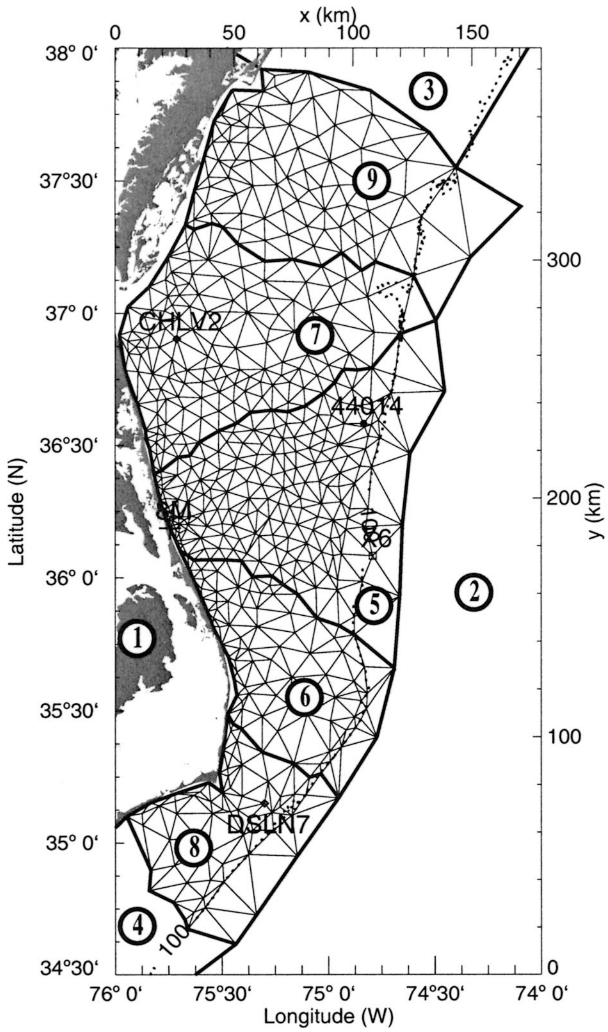

FIG. 4. Model grid. The grid points from which rays are traced backward and where the source terms are evaluated are the nodes of the triangular mesh. A linear interpolation is applied in each triangle to approximate the source terms along the rays. The entire model domain is divided into subdomains, numbered 1–9, separated by thicker lines. The locations of some instruments are added for geographical reference, and a dotted line marks the 100-m depth contour.

eraged over a bundle of rays spanning a finite band of frequencies and arrival directions. The source terms in (2) are determined from the spectrum at each grid point and interpolated in space and direction on the rays.

b. Bathymetry and model grid

In order to encompass all the instrumented sites and allow for oblique swell arrivals, the model domain was set to cover the North Carolina and Virginia shelf, extending 400 km between 34°30′N, south of Cape Hatteras, and 38°N, at the Virginia–Maryland border on Assateague Island (Fig. 4). The National Ocean Service (NOS) database of depth soundings in that region generally has a resolution better than 200 m, with finer details resolved around shoals dangerous for navigation. A large gap in this dataset, off Duck between X2 and X5, was filled with soundings acquired during various instrument deployment, maintenance, and recovery cruises on board the R/V *Cape Hatteras* from 1994 to 1999. High-resolution multibeam sonar surveys were conducted during SHOWEX with a Simrad EM1000 system on board the Canadian Hydrographic Vessel *Frederick G. Creed* (M. Donelan et al. 1999, personal communication), and with an ISIS 100 system mounted on the side of the R/V *Cape Hatteras* (J. McNinch and T. Drake 2000, personal communication). This composite dataset was gridded with 6″ resolution in latitude and longitude (180 and 150 m, respectively). Before computing wave rays, the bathymetry was smoothed with an isotropic tapered filter with a radius equal to 5 times the local wavelength (adapted to the wave frequency and local water depth) in order to remove the small scale topographic features that are represented in a stochastic form in the wave–bottom Bragg scattering source term. The unstructured model grid was constructed starting from the instrument positions. Points were added along isobaths at 8, 15, 20, 25, 30, 40, 60, 100, and 1500 m with increasing spacing away from the coast and away from the instrumented transects. The resolution of this irregular grid was increased gradually introducing new points at the centers of the corresponding Delaunay triangles, until all sides of these triangles were shorter than 2–20 km (depending on the water depth and the alongshore location). The model uses 29 frequency bands from 0.05 to 0.15 Hz and 72 direction bands regularly spaced at 5° intervals. For each of these finite bands, bundles of rays were traced from all grid points. To reduce the large computational effort, the ray computations were stopped and energy fluxes were interpolated at the boundaries of nine model subdomains (numbered from 1 to 9 in Fig. 4) [see Ardhuin et al. (2001) for further details].

c. Boundary conditions

At the external boundaries bordering subdomains 1 (land), 2 (offshore), 3 and 4 (north and south model limits) the following conditions are applied. The offshore frequency–direction wave spectrum is interpolated from estimates at X6 and 44014, back-refracted to deep water, assuming parallel bottom contours. Although the offshore conditions generally varied slowly on timescales of several hours, the deep water spectra are interpolated at 10-min intervals in order to match the model time step Δt. To account for advection time lags between the boundary grid points and the offshore measurement locations, at each grid point, each interpolated frequency–directional wave component was shifted in time by the delay corresponding to the projection, on its propagation direction, of the distance to the measurement location, using the deep water group speed of linear waves. This procedure was used also for

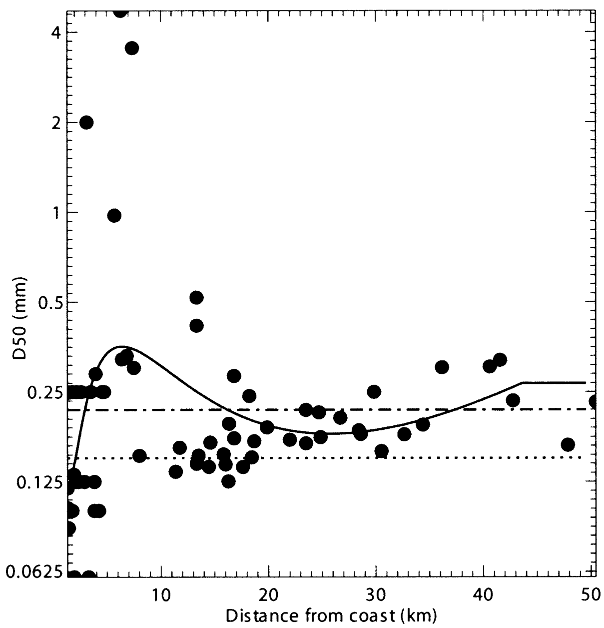

FIG. 5. Median grain sizes D_{50} of surficial sediments as a function of distance from the coast. Filled circles indicate analysis results of vibracore samples collected in the period 1994–97 (R. Beavers, Duke University, 1999, personal communication), and Shipek grab samples collected during SHOWEX. The dotted line indicates $D_{50} = 0.15$ mm, used by Ardhuin et al. (2001) in previous hindcasts. The average grain size $D_{50} = 0.22$ mm is indicated by the dash–dotted line, and the solid line is a polynomial fit used in the present hindcasts, with a constant value offshore.

the lateral boundary conditions (between subdomains 4 and 8, 9 and 3: see Fig. 4), crudely accounting for refraction of the offshore spectrum by assuming an alongshore uniform shelf and applying Snel's law. This treatment of the lateral boundaries does not represent accurately the propagation of waves across shelf regions outside the model domain, but avoids artificial shadow regions created by closed lateral boundaries. At the coastal boundary, bordered by land and narrow inlets (domain 1), a zero incoming energy flux is prescribed, neglecting weak wave reflection from beaches, and wave propagation from the inland sounds to the open ocean through the inlets.

d. Bottom sediments and small-scale topography

Qualitative inspection of 20 sediment core samples collected in 1997 on the inner shelf (R. Beavers, Duke University, 1999, personal communication) and quantitative grain size analysis of 50 samples gathered during SHOWEX (Ardhuin et al. 2002a) give a good description of surficial sediments in a narrow (20 km wide) region around the 8M–X5 transect (Fig. 5). The median grain diameter D_{50} varies between 0.09 and 4 mm, with the finest sediment within 2 km from shore and the coarsest sediment in low-lying areas 2–15 km from shore. The average value of D_{50} (binned as a function of distance from shore) is 0.22 mm, slightly coarser than the average D_{50} (0.15 mm) used by Ardhuin et al. (2001). In order to extrapolate these observations away from the 8M–X5 transect, a fifth-order polynomial was fitted to the distribution of D_{50} as a function of the logarithm of the distance from shore (Fig. 5). This fitted distribution is used here to evaluate the movable bed friction source term. However, very similar results in model hindcasts obtained with a uniform value $D_{50} =$ 0.22 mm suggest that the model is insensitive to these spatial variations in median grain size.

The small-scale bottom topography, potentially important for scattering waves, is generally well resolved in the NOS bathymetric database down to scales ($2\pi/l$, with l the bottom wavenumber) of about 300 m, in water depths between 10 and 30 m, with a variance that decreases by a factor of 3 from inner-shelf shoals to midshelf regions. The corresponding two-dimensional wavenumber spectra are not isotropic and show a concentration of variance at wavenumbers aligned with a northwest to southeast axis (e.g., Fig. 6a). For wavelengths under 300 m, the topography is resolved only in the multibeam surveys conducted in two small regions, in 20- and 25-m depth (Ardhuin and Herbers 2002, Figs. 8 and 9). The direction-integrated spectra, indicated with dashed lines in Fig. 6, again show higher levels at the shallower site, but the shapes are similar with an l^{-3} roll off extending down to wavelengths of 50 m. All observed spectra obtained from additional individual track surveys (not shown) also roll off as l^{-3}, with variance levels in the range of those shown in Fig. 6.

Because the detailed variability of topographic features that contribute to wave–bottom Bragg scattering (with horizontal scales smaller than about 5 times the surface wavelength) was not measured across the entire study region, a single representative bottom elevation spectrum for the shelf was constructed from the survey data. Average spectral levels at the larger scales were obtained from the 6′ resolution bathymetry grid, ensemble averaging over regions with water depths between 10 and 30 m (Fig. 6a and solid line in Fig. 6b). These average spectral levels are lower than those estimated in regions with well-resolved shoals (dotted lines in Fig. 6b), possibly due to artificial smoothing of the grid (obtained by triangulation) in deeper regions where depth soundings are sparse. At higher wavenumbers ($l/2\pi > 0.002$ m^{-1}), not resolved by the 6″ grid, the spectral levels were taken from the high-resolution spectrum estimate on the inner shelf (Ardhuin and Herbers 2002, Fig. 8). Although computations of Bragg scattering presented below do not account for the variability of spectral levels and directional properties of the bottom topography, the cumulative effect of the shelf topography on swell transformation across the shelf should be well quantified by this composite spectrum.

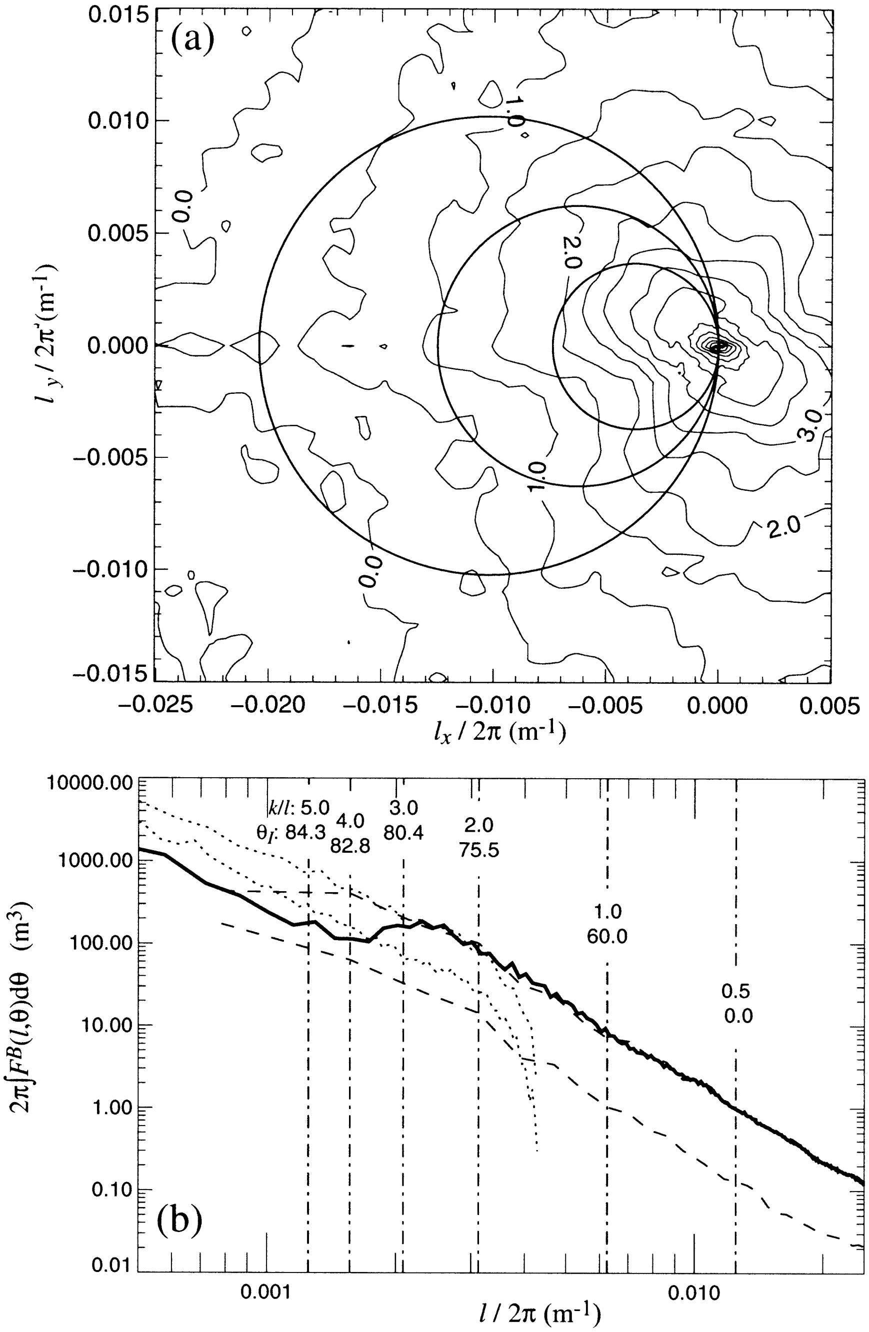

FIG. 6. (a) Composite two-dimensional bottom elevation spectrum F^B, based on 10–30-m-depth bathymetry in the entire model domain and high-resolution multibeam bathymetry in a 5 km × 5 km region in 20-m depth. Contour values are $\log_{10}(4\pi^2 F^B)$, with F^B in m^4 rad^{-2}, at 0.5 intervals. Circles indicate the bottom components at 20-m depth that interact with waves from the east with frequencies 0.05 (inner circle), 0.12 (middle circle), and 0.25 Hz (outer circle). Axes units are reciprocal wavelengths $l_x/(2\pi)$ and $l_y/(2\pi)$. (b) Corresponding direction-integrated spectrum (solid). Also shown are various omnidirectional spectra estimated from high-resolution multibeam bathymetry (dashed) and-well resolved regions in the NOS database (dotted). The vertical lines indicate the bottom scales responsible for scattering 0.08-Hz swell at different incidence angles θ_I, with resonant surface wave–to–bottom wavenumber ratios k/l ranging from 0.5 to 5.

e. Source terms

The wave–bottom Bragg scattering source term S_{Bragg} takes the form given by Ardhuin and Herbers (2002),

$$S_{\mathrm{Bragg}}(\mathbf{k}) = \omega K(k, H) \int_0^{2\pi} \cos^2(\theta - \theta') k^4 F^B(\mathbf{k} - \mathbf{k}') \times [E(\mathbf{k}') - E(\mathbf{k})]\, d\theta', \quad (3)$$

where the radian frequency ω is related to k by the linear dispersion relation

$$\omega = gk \tanh(kH), \quad (4)$$

θ and θ' are the directions of the surface wavenumber vectors $\mathbf{k}$ and $\mathbf{k}'$ respectively, H is the local water depth, and K is a nondimensional coupling coefficient,

$$K(k, H) = \frac{4\pi}{\sinh(2kH)[2kH + \sinh(2kH)]}. \quad (5)$$

Here S_{Bragg} is estimated using a bottom elevation spectrum F^B that is uniform across the shelf and integrated with a semi-implicit scheme, taking advantage of the linear relationship between E and S_{Bragg} (Ardhuin and Herbers 2002).

Following earlier work by Madsen et al. (1990) and Tolman (1994), we use a parameterization of the bottom friction source term S_{fric} that is quasilinear in the wave spectrum with a variable dissipation factor f_e that depends on the hydraulic seabed roughness. Defining a_b and u_b as the root-mean-square (rms) amplitudes of the wave orbital displacement (one-half of the orbital diameter) and the velocity at the top of the boundary layer, S_{fric} is parameterized as

$$S_{\mathrm{fric}}(\mathbf{k}) = -f_e u_b E(\mathbf{k}) \frac{(2\pi f)^2}{2g \sinh^2(kH)}, \quad (6)$$

where f_e is given as a function of a_b and the bottom Nikuradse roughness length k_N, using Grant and Madsen's (1979) boundary layer model for an equivalent monochromatic wave with a linear eddy viscosity profile.

We use a slightly modified version of Tolman's decomposition of k_N in a ripple roughness k_r and a sheet flow roughness k_s [Tolman (1994), based on previous work by Grant and Madsen (1979), Wilson (1989), and Madsen et al. (1990)],

$$k_r = a_b \times A_1 \left(\frac{\psi}{\psi_c}\right)^{A_2} \quad (7)$$

$$k_s = 0.57 \frac{u_b^{2.8}}{[g(s - 1)]^{1.4}} \frac{a_b^{-0.4}}{(2\pi)^2}. \quad (8)$$

In (7) A_1 and A_2 are empirical constants, s is the sediment specific density, and g is the gravity acceleration; ψ is the Shields number determined from u_b and the median sand grain diameter D_{50},

$$\psi = f'_w u_b^2 / [g(s - 1)D_{50}], \quad (9)$$

with f'_w the friction factor of sand grains (determined in the same way as f_e with D_{50} instead of k_r as the bottom roughness), and ψ_c is the critical Shields number for the initiation of sediment motion under sinusoidal waves on a flat bed. We use an analytical fit (Soulsby 1997) to Shields's (1936) laboratory data:

$$\psi_c = \frac{0.3}{1 + 1.2D_*} + 0.055[1 - \exp(-0.02D_*)], \quad (10)$$

$$D_* = D_{50}\left[\frac{g(s - 1)}{\nu^2}\right]^{1/3}, \quad (11)$$

where ν is the kinematic viscosity of water. This expression is consistent with the laboratory data reviewed by Madsen and Grant (1976) and the ripple roughness parameterization of Madsen et al. (1990), although recent experimental results for mixed sands suggest somewhat larger values of ψ_c (Wallbridge et al. 1999). Grant and Madsen's (1979) boundary layer theory provides a friction factor f_w (relating the stress to the velocity) rather than a dissipation factor f_e, but Madsen et al. (1990) measured wave attenuation and thus dissipation, rather than stresses, to find a parameterization for k_r. It is thus consistent to use f_e in (6) when using the parameterization (7).

When the wave motion is not strong enough to generate vortex ripples, that is, for values of the Shields number less than a threshold ψ_{rr}, k_N is given by a relic ripple roughness k_{rr}. Madsen et al. (1990) proposed

$$\psi_{\mathrm{rr}} = A_3 \psi_c, \quad (12)$$

with $A_3 = 1.2$ determined in laboratory experiments with random waves. In the absence of any bedform data, Graber and Madsen (1988) set the relic ripple roughness k_{rr} equal to D_{50}, which is appropriate for a flat bed composed of well-sorted sand. Tolman (1994) suggested a generally larger constant value $k_{\mathrm{rr}} = 0.01$ m to account for relic bedforms and bioturbation. Hindcasts of the evolution of small waves ($H_s < 1$ m) across the North Carolina shelf support these small roughness values, but the inferred dissipation was too weak to reliably quantify k_{rr} (Ardhuin et al. 2001). In this paper we present hindcasts of waves on the North Carolina shelf (almost entirely covered with noncohesive sand) that suggest that the roughness may increase with the forcing, possibly due to the presence of relic bedforms that are more likely to be intercepted by larger orbital diameters a_b. We propose a simple linear relation:

$$k_{\mathrm{rr}} = \max\{0.01 \text{ m}, A_4 a_b\} \quad \text{for } \psi < \psi_{\mathrm{rr}}. \quad (13)$$

The practical use of bedform roughness parameterizations is complicated further by spatial variations of the water depth and sediment grain size (see for example Green 1986) on scales not resolved by operational wave prediction models. In order to apply the local parameterization to a larger scale, we use a statistical representation of subgrid variations in water depth (Ardhuin et al. 2001; adapted from Tolman 1995). Additional tests with a subgrid representation of variations in median grain sizes, did not give significantly different results.

The general bed roughness parameterization (6)–(13) contains four empirical coefficients. The values $A_1 = 1.5$, $A_2 = -2.5$, $A_3 = 1.2$, and $A_4 = 0$ proposed by Tolman [(1994), based on laboratory experiments by Madsen et al. (1990)] yield remarkably accurate predictions of wave height decay over a wide range of forcing conditions [Ardhuin et al. (2001) and Part II]. It is shown in Part II that slightly different values ($A_1 = 0.4$ and $A_2 = -2.5$, $A_3 = 1.2$, and $A_4 = 0.05$) increase the overall hindcast skill, and these tuned coefficients are used in the analysis of swell events presented below.

5. Observations and model hindcasts

Wave data and model hindcasts are presented here for four swell events that include a wide range of wave heights, periods, and directions, revealing different evolution patterns across the shelf. Periods were selected when the local wind speed on the shelf was significantly smaller (less than 60%) than the propagation speed of the dominant waves and thus the local wind generation effects on the energy balance can be neglected (see Part II for details). The importance of different physical processes can be evaluated by turning the corresponding source terms on and off in model hindcasts. This approach is particularly useful in sorting out processes that have similar effects, such as the decrease in wave height toward the shore caused by both refraction and bottom friction. Here model results without any source terms (run 1, including only the effects of shoaling and refraction) and runs with both bottom friction and Bragg scattering (run 4c) are compared. Hindcasts with other combinations and alternative formulations of source terms are presented in Part II. In addition to model–data comparisons of the significant wave height (H_s) decay, which is believed to be caused primarily by bottom friction (and refraction for large oblique swell arrival angles), the cross-shelf evolution of a mean propagation direction and directional spread are examined to test predictions of refraction and scattering effects. The model spectral densities are transformed to frequency–directional space

$$E(f,\ \theta) = kE(\mathbf{k})/(2\pi C_g),$$

for comparison with observations. We define a mean wave direction θ_p at the peak frequency f_p (defined as direction from in nautical convention), using an energy-weighted average over a finite bandwidth of 0.15 f_p centered at f_p. Following standard conventions (e.g., Kuik et al. 1988), θ_p is defined as the direction of the first-order moment vector,

$$(a_{1,p},\ b_{1,p}) = \frac{\displaystyle\int_{0.925f_p}^{1.075f_p}\int_0^{2\pi}(\cos\theta,\ \sin\theta)E(f,\ \theta)\ d\theta\ df}{\displaystyle\int_{0.925f_p}^{1.075f_p}\int_0^{2\pi}E(f,\ \theta)\ d\theta\ df}. \quad (14)$$

Here f_p is determined from the measured frequency spectra at X1 so that the modeled and observed directions correspond to the exact same frequency band. The directional spread at the peak frequency $\sigma_{\theta,p}$ is computed for each instrument in the same way, based on the conventional definition, in radians,

$$\sigma_{\theta,p} = [2(1 - a_{1,p}\cos\theta_p - b_{1,p}\sin\theta_p)]^{1/2}, \quad (15)$$

where $\sigma_{\theta,p}$ is an estimate of the standard deviation of the directional distribution of wave energy, and thus can be loosely interpreted as the half-width of the directional spectrum (e.g., Kuik et al. 1988). The maximum value of $\sigma_{\theta,p}$, for an isotropic spectrum, is $2^{1/2}$ radians, that is 81°.

a. Attenuation of small to moderate swells

Small-amplitude swell from the east, with an offshore $H_s \approx 0.6$ m and $f_p \approx 0.08$ Hz, were observed on 18–19 November when local winds were very weak (about 3 m s^{-1}). On 20 November (discarded for analysis) wind speeds increased briefly to 7 m s^{-1}, followed by a 5-day period of steady, light (5 m s^{-1}) winds, during which the offshore swell H_s increased to 2.0 m, with a nearly constant f_p of about 0.09 Hz.

Initially when the offshore H_s was less than 1.3 m, measured wave heights at all inner shelf sensors were close to the offshore (X6 and 44014) observations (Fig. 7), and mean directions (not shown) were nearly constant across the shelf, except for some refraction inshore of X1. The model hindcast for these small waves is dominated by local refraction and shoaling effects that cause primarily alongshore variations in wave height with strong amplification on shoals south of CHLV2 and around Cape Hatteras, and no significant attenuation across the shelf (Fig. 8a). In the model hindcasts, both bottom friction and Bragg scattering have a negligible effect on H_s (Fig. 7). Significant differences between H_s observations at outer shelf buoys X6 and 44014 (about 25%; Fig. 8b), indicate alongshore variations of the deep water incident wave field that are possibly caused by refraction over the Gulf Stream and its meanders that dominate the offshore ocean circulation in this area (e.g., Holthuijsen and Tolman 1991), and natural spatial fluctuations of a wave field initially generated by nonhomogeneous winds (Tournadre 1993).

With larger offshore wave heights on 22–26 November, significant differences are observed between the narrow shelf region around Cape Hatteras and the wider shelf in the vicinity of the Chesapeake Bay entrance. At DSLN7, in shallow water near Cape Hatteras, H_s varies between 1.5 and 1.7 m (Fig. 7a), close to the

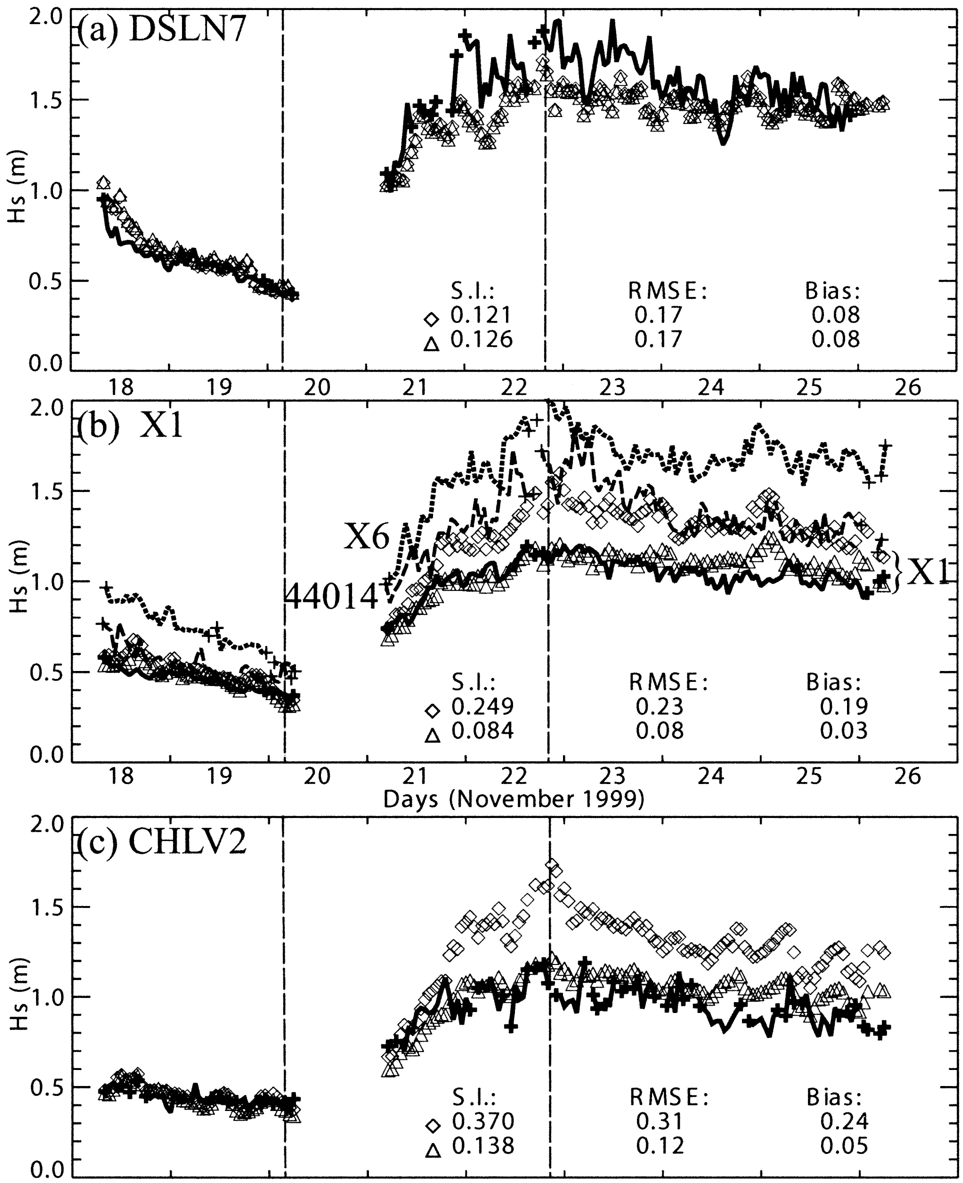

FIG. 7. Observed (solid) and predicted (diamonds: no source terms; triangles: with source terms) significant wave heights H_s at (a) DSLN7, (b) X1, and (c) CHLV2. Offshore wave heights are indicated in (b) for reference (dashed: 44014; dotted: X6). Lines are interrupted with + symbols when data are missing or the record is discarded owing to significant local wind effects. The model scatter index (S.I.), rms error (RMSE), and bias are indicated.

offshore wave heights, whereas H_s is reduced to about 1.0 m at sites X1 and CHLV2 (Figs. 7b,c) located inshore of a wide shelf. These observations are in agreement with the predicted cumulative effect of bottom friction across a wide shelf. Indeed, the model hindcast that includes no source terms (representing only refraction and shoaling) overestimates wave heights at X1, CHLV2 (diamonds in Figs. 7b,c) and all other inner shelf sensors, while the addition of source terms brings the predicted wave heights in close agreement with observations. The scatter index (SI), defined as

$$\mathrm{SI}(H_s) \equiv \left[\frac{\sum_i (H_{s,\mathrm{obs},i} - H_{s,\mathrm{pre},i})^2}{\sum_i H^2_{s,\mathrm{obs},i}}\right]^{1/2}, \tag{16}$$

with $H_{s,\mathrm{obs},i}$ and $H_{s,\mathrm{pre},i}$ the observed and predicted values of H_s at time t_i, is reduced from 0.25 to 0.08 at X1 for the 18–26 November period when source terms are included (Fig. 7b).

As waves propagate toward the shore, strong attenuation is first noticed at the lower frequencies (Fig.

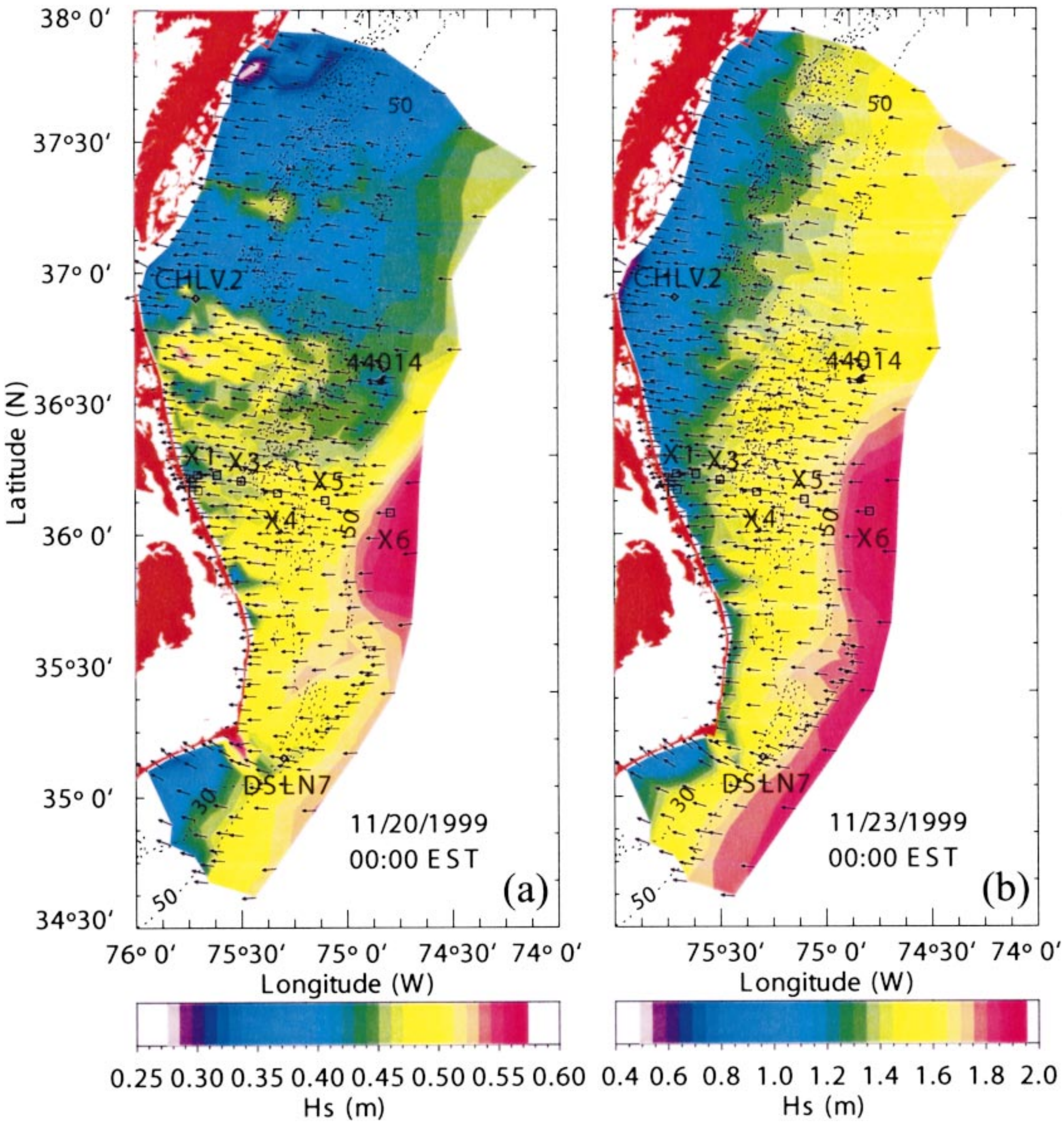

FIG. 8. Predicted (model run 4c, with source terms) wave heights H_s (colors) and mean directions θ_p (arrows) at 0000 EST on (a) 20 Nov 1999 and (b) on 23 Nov 1999.

9). As a result the spectral peak becomes less steep on the low-frequency side and more symmetric, causing a slight shift of f_p to higher frequencies. Although the spectral representation of bottom friction in the model is heuristic, the predicted evolution of frequency spectra agrees fairly well with observations (Fig. 9). Wave energy dissipation by bottom friction over relic bedforms appears to be well represented by the quasilinear formulation with a single bottom roughness length for all wave frequencies, similar to dissipation over active bedforms, confirming previous studies by Mathisen and Madsen (1999) and Ardhuin et al. (2002b).

The absence of any measurable dissipation when offshore wave heights are less than 0.8 m supports the current parameterization of bottom friction with a very small roughness for low Shields numbers. However, H_s is reduced by 20%–30% (in comparison with the model hindcast without source terms) for moderate offshore wave heights (e.g., 1.5 m on 21 and 24–26 November) that are not energetic enough to form vortex ripples. This result suggests that significant dissipation can occur over relic bedforms and that the relative attenuation of wave energy increases gradually with increasing wave height in the relic ripple regime.

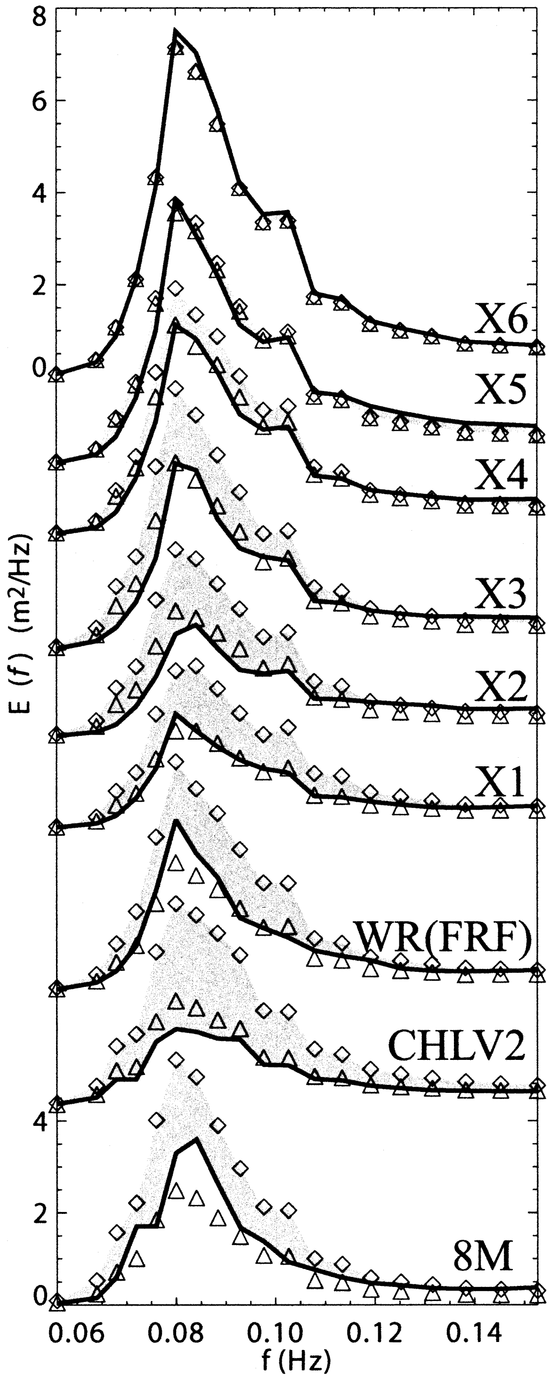

FIG. 9. Evolution of wave frequency spectra (12-h averages) across the shelf on 22 Nov (solid) are compared with model hindcasts (diamonds: no source terms; triangles: with source terms). The shaded area highlights the difference between observation and model hindcast without source terms, that is, the cumulative spectral decay caused by dissipation of wave energy on the shelf. Plots are offset vertically for each site. The spectral estimates have 432 degrees of freedom (for 0.1 Hz), corresponding to a 10% error at the 95% confidence level.

b. Hurricane Floyd

Before landfall, Hurricane Floyd generated large swells that arrived at the shelf break at large oblique southerly angles. During the morning of 15 September, as the eye of the hurricane was moving north along the Florida Peninsula, a near-grazing arrival direction of $\theta_p = 161°$ was measured at buoy X6, with a wave height $H_s = 2.8$ m and a peak frequency $f_p = 0.07$ Hz. Weak local winds measured at the experiment site (less than 6 and 5 m s^{-1} at the FRF pier and buoy 44014, respectively) suggest that the evolution of these long-period waves across the shelf was not significantly affected by local winds. This was confirmed by model runs, not described here, using source terms for wind generation, nonlinear evolution, and whitecapping.

Owing to the large distance (about 1000 km) between the storm and the experiment site, and partial sheltering by Cape Hatteras, the directional wave spectrum was very narrow, with a spread at the peak frequency $\sigma_{\theta,p}$ of 13° at the offshore buoy X6. The measured swell evolution across the shelf shows a reduction of H_s from 2.8 m at X6 to 1.7 and 1.2 m at X1 and 8M, respectively, and a large change in the mean direction θ_p from 161° at X6 to 115° and 95° at X1 and 8M, respectively. The relatively small difference in H_s between X6 and X1 is explained by the focusing of waves over inner shelf shoals, caused by refraction, yielding an increase in wave heights between X3 and X2 in the frictionless model hindcast (Fig. 10a). This effect partly compensates for energy losses caused by bottom friction, followed by a strong reduction across the inner shelf. The refraction over two-dimensional topography is also evident in the cross-shelf evolution of θ_p, showing a slight veering to a more southerly direction across the mid shelf (from 140° at X5 to 145° at X4), before shifting toward shore-normal incidence with accompanying reductions in wave heights at WR(FRF) and 8M. This pattern is well represented in the frictionless model calculations (run 1, Fig. 10c).

Model predictions of H_s that account for bottom friction agree well with observations at all sites with only a slight (20–40 cm) underprediction of H_s between X4 and 8M (Fig. 10b). Observed variations of $\sigma_{\theta,p}$ across the shelf from X6 to 8M are relatively small, and this small change of $\sigma_{\theta,p}$ is reproduced well by the model hindcast with source terms (run 4c), while the model run without source terms (run 1) predicts a dramatic narrowing (down to 5° at 8M) that is not observed. The near uniformity of observed $\sigma_{\theta,p}$ thus masks a balance between a narrowing due to refraction and a broadening due to Bragg scattering (Fig. 10d).

Whereas the overall trend in the cross-shelf evolution of the directional spectrum is well represented by the model with source terms, significantly larger spreads are observed at WR(FRF), X5, and 44014. Such differences may be caused by local refraction effects, as narrow spectra are sensitive to bottom to-

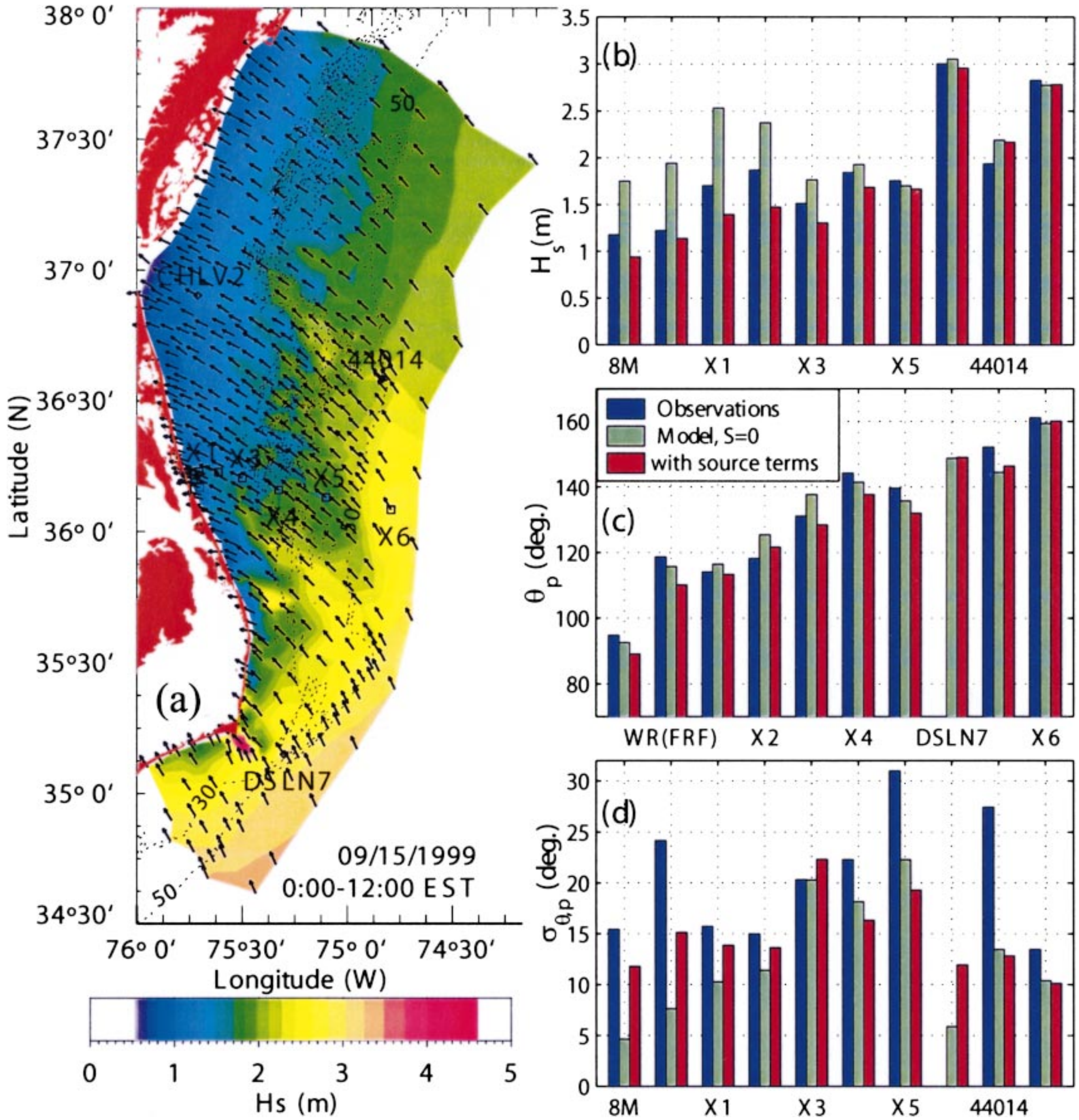

FIG. 10. Hurricane Floyd swell: (a) predicted (with source terms) wave heights H_s (colors) and mean directions θ_p (arrows); (b)–(d) observations and predictions (with and without source terms) of H_s, θ_p, and $\sigma_{\theta,p}$ at all instrumented locations. All parameters are averages over a 12-h period from 0000 to 1200 EST 15 Sep 1999.

pographic details. However, the bathymetry near the instrument sites should be well resolved in the present model. Lack of directional resolution in the offshore wave measurements (X6 and 44014) used to drive the model and unresolved spatial variations in the offshore wave conditions may also contribute to these discrepancies.

c. Hurricane Gert

Shortly after the passage of Hurricane Floyd, large swells (H_s in the range 2–3 m at X6 and $f_p = 0.07$ Hz) arrived from the southeast, generated by Hurricane Gert (Fig. 3). Again a large reduction in H_s was observed across the wide and shallow shelf near Chesapeake Bay, from 2.0–3.5 m at offshore buoys 44014 and X6 to about 1.0 m at X1 and CHLV2 (Figs. 11b,c), whereas virtually no attenuation is observed near Cape Hatteras where the shelf is narrow (DSLN7, Fig. 11a). The model hindcast without source terms predicts values of H_s at CHLV2 that are slightly larger than at X6 owing to shoaling and refraction in the shoal area where the instrument is located. In contrast waves are attenuated by refraction at X1 as their propagation direction turns toward the obliquely oriented coastline (compare diamonds and to offshore observations in Fig. 11). Sites

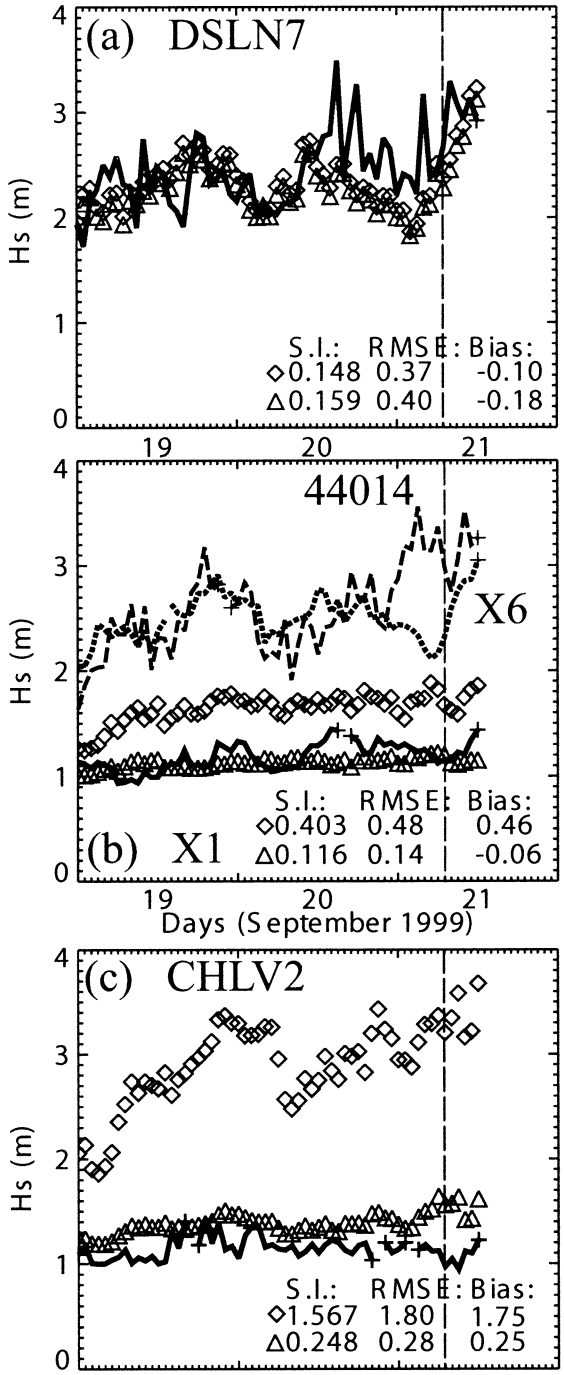

FIG. 11. Same as Fig. 7, but for the period 19–21 Sep (Hurricane Gert).

DSLN7, X1, and CHLV2 are in similar water depths (18, 21, and 15 m, respectively), but the difference between linear refraction predictions (diamonds in Fig. 11) and observations (solid lines) vary from very good agreement at DSLN7 to overpredictions of 50% and 200% at X1 and CHLV2. These large differences reflect the cumulative dissipation of wave energy across the shelf, which is negligible across the 10-km-wide shelf at DSLN7 while CHLV2 is sheltered by a shallow shelf region 100 km wide. Although water depths offshore of these instruments are too large to cause depth-induced breaking for these swells, model predictions that include the source terms reproduce accurately the wave heights observed at the inner shelf sites.

The strong dissipation rates predicted offshore of CHLV2 (Fig. 12) are due to the sharp increase in the bed hydraulic roughness when sand ripples are formed. Large ripples were indeed observed in sidesscan sonar surveys on 26–29 September over most of the X1–X5 transect, a few days after Gert swells were recorded. Observed ripple wavelengths in the range 0.5–3 m, and ripple crests facing directions from 70° to 100°, differ from previous surveys on 10–13 September, and are consistent with the propagation directions and near-bed orbital diameters of Gert swells (Ardhuin et al. 2002a). These results reveal the remarkable sheltering effect of a wide shelf for the coastal zone. Whereas the narrow shelf at Cape Hatteras causes negligible wave attenuation, the wide and shallow shelf offshore of Chesapeake Bay dissipates up to 93% of the onshore wave energy flux, these large energy losses (about 100 kW per meter of coastline) are the result of a weak dissipation (1 W m^{-2}) distributed over a shelf region 100 km wide (Fig. 12b).

Directional properties were observed to vary significantly in time and space during this event. The general refraction pattern across the shelf shows the expected gradual shift of θ_p toward the normal to the depth contours, that is, 70° at the beach (Fig. 12a). However, the unusually narrow directional spectra observed during this event amplified local refraction effects, causing large alongshelf gradients in wave height (Fig. 12a) and large variations of θ_p on the shelf. For example, at site X5 θ_p fluctuated between 97° and 138°, whereas θ_p at X6 varied only between 120° and 130° (Fig. 13a). The model predicts the general turning of θ_p across the shelf (e.g., the good agreement with observations at X3 and X2) but overpredicts refraction at inner shelf sites 8M and X1 (θ_p = 90° in the hindcast when θ_p = 120° is observed) and does not predict the large variations of θ_p observed at X5. Some discrepancies may result from unresolved local refraction, but these errors are expected to be small on the inner shelf because the bathymetry between X1 and X2 is resolved well in the multibeam sonar surveys conducted during SHOWEX (Ardhuin and Herbers 2002). A more likely source of error is the specification of the offshore boundary condition, either because the offshore wave field is not homogeneous or because the directional spectra reconstructed from the buoy data using the maximum entropy method (Lygre and Krogstad 1986) may be significantly different from the actual offshore wave spectra. A large difference between θ_p at X6 and 44014 was occasionally observed (Figs. 14b,c) even though the source of these waves,

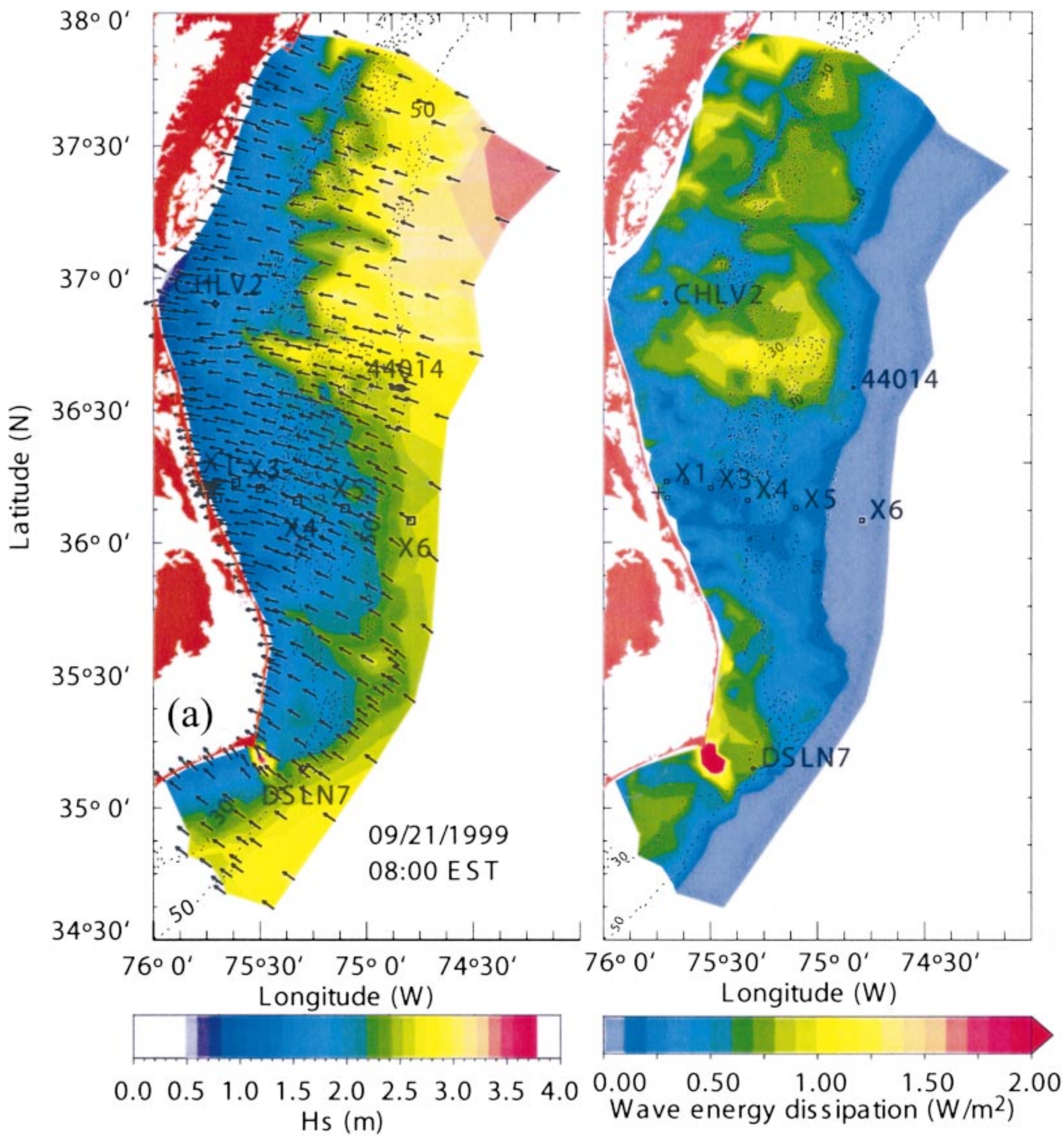

FIG. 12. (a) Predicted (with source terms) wave heights H_s (colors) and mean directions θ_p (arrows) at 0800 EST 21 Sep 1999, and (b) corresponding energy dissipation rates based on the parameterization of bottom friction over a movable bed.

Hurricane Gert, was over 2000 km offshore (Fig. 3). This difference, possibly due to refraction over the Gulf Stream or associated eddies, suggests that comprehensive observations of the offshore wave field are necessary for a more quantitative evaluation of the model parameterizations.

Narrow offshore swell directional spectra were again observed to broaden across the shelf (Fig. 13c), in particular with very low ($<$0.07 Hz) peak frequencies (Fig. 13d). In the afternoon of 19 September, $\sigma_{\theta,p}$ increased from 13° at X6 to 28° at X1, and this dramatic broadening is reproduced well by the hindcast that includes wave–bottom Bragg scattering (Fig. 13c, triangles).

6. Conclusions

New observations of the attenuation and directional transformation of waves across the North Carolina continental shelf were obtained over a three-month period during the 1999 Shoaling Waves Experiment. Observations in swell-dominated conditions confirm previous observations of strong attenuation of large swells across the wide and shallow shelf, with typical wave height reductions of a factor of 2, and relatively weak variations for small swells with $H_s < 1.0$ m offshore. Comparisons with energy-conserving linear refraction calculations show that this attenuation can sometimes be

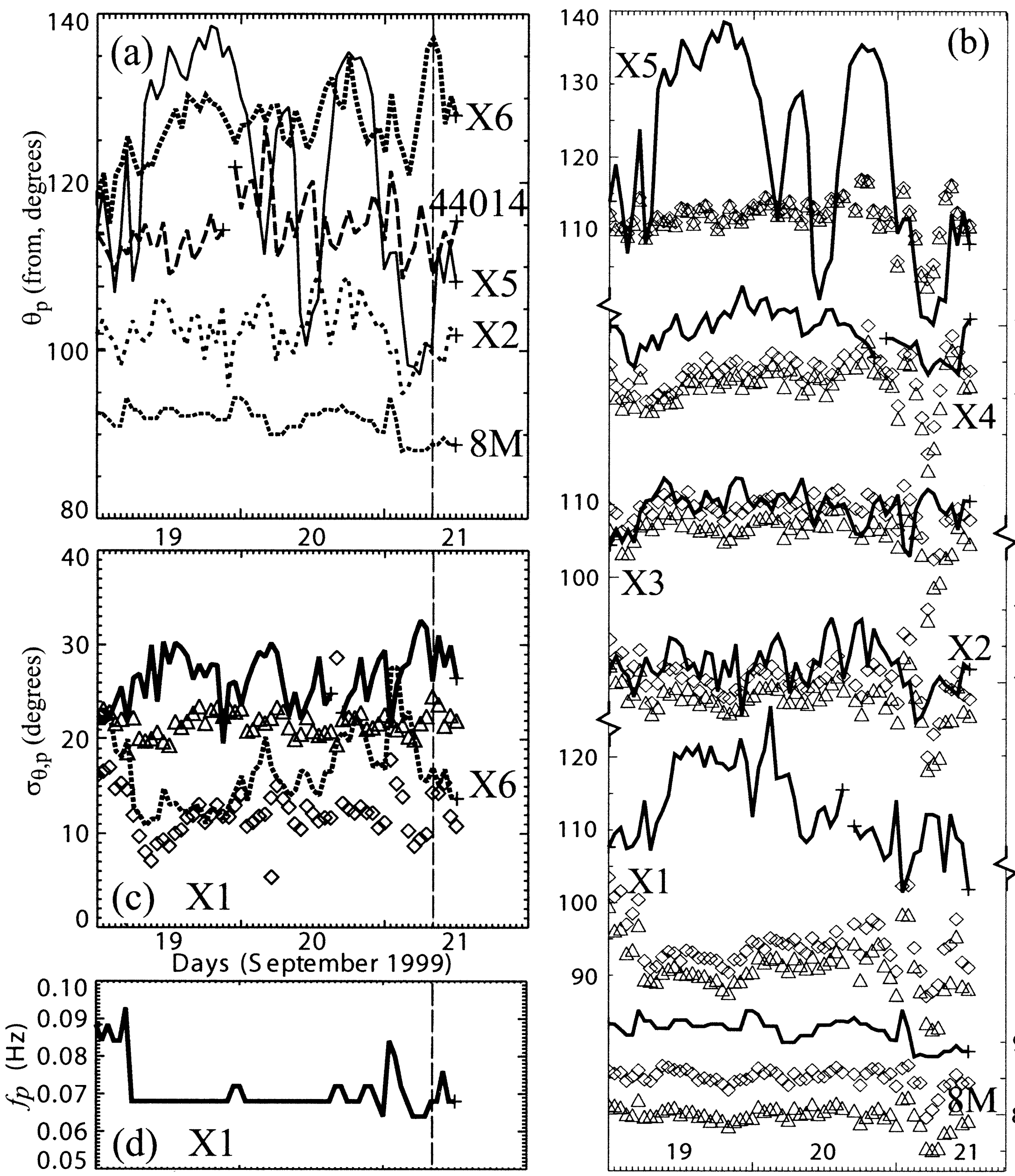

FIG. 13. Directional properties of Hurricane Gert swell: (a) observed mean wave direction θ_p, at several sensors from X6 (offshore) to 8M (8-m depth); (b) comparison of observed θ_p (solid lines) with model predictions without source terms (diamonds) and model predictions with source terms (triangles). Plots are offset for each site, and axes alternate between left (for X1, X3, X5) and right (for 8M, X2, X4). (c) Comparison of observed directional spread $\sigma_{\theta,p}$ at X1 (solid) with model hindcasts (diamonds: no source terms; triangles: with source terms). The offshore directional spread observed at buoy X6 is indicated with a dotted curve. (d) Peak frequency f_p at X1.

partially attributed to refraction, in particular when waves arrive at large oblique angles with respect to the shoreline. However, the strong decay of energetic swell in the absence of local winds suggests that dissipation of wave energy by bottom friction is the primary attenuation mechanism. The inferred swell damping across the shelf is negligible near Cape Hatteras where the shelf is narrow and maximum near Chesapeake Bay where the shelf is wide and shallow. For the largest observed swells, from Hurricane Gert, H_s is reduced by up to 74% near the mouth of Chesapeake Bay, corresponding to a reduction of the incident wave energy flux by 93%.

The highly variable attenuation is reproduced well by a parameterization of bottom friction over a movable sandy bed that represents large changes in bottom

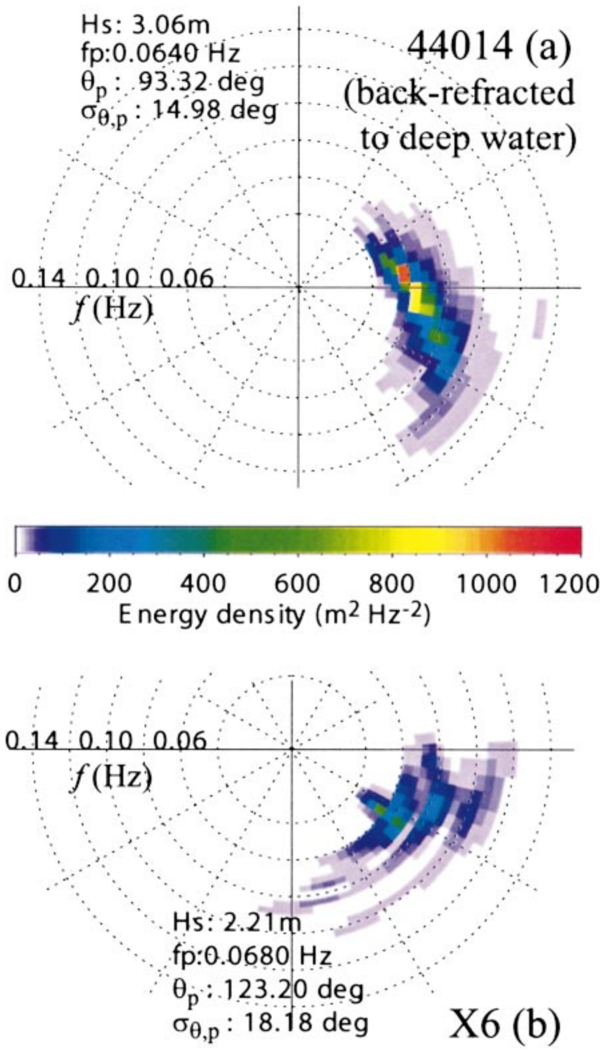

FIG. 14. Estimated frequency-directional spectra at the offshore buoys (a) 44014 and (b) X6 at 0800 EST 21 Sep 1999.

roughness associated with the formation of sand ripples. Hindcasts of the spectral energy balance of swell on the shelf were performed using a formulation of the bottom friction source term proposed by Tolman (1994) with a modification of the empirical coefficients determined by Madsen et al. (1990) in the laboratory. Results accurately reproduce the weak swell decay in low energy conditions, strong decay in high energy conditions, and the dependence of the decay on shelf width. These results lend strong support for the dominant role of bottom friction in swell transformation across continental shelves and the dramatic sheltering of a wide shelf for the nearshore environment. The present swell measurements only included significant wave heights less than 4 m. For larger waves, the sheltering effect of the shelf may become less efficient as the bottom roughness is reduced when a rippled seabed transitions to sheet flow [e.g., the 1994 Hurricane Gordon discussed in Ardhuin et al. (2001)].

The half-width $\sigma_{\theta,p}$ of the directional spectrum at the peak frequency was observed to be fairly constant across most of the shelf, increasing toward the shore for narrow offshore spectra, and decreasing only slightly for broad offshore spectra. This observation is contrary to linear refraction theory, which generally predicts that the wave spectrum narrows around the direction normal to the depth contours as waves approach the shore. However, Bragg scattering of waves by bottom topographic features with horizontal scales of the order of a few wavelengths (forward scattering) provides a natural diffusion mechanism that opposes refraction, and the model hindcast that includes this process yields an onshore increase of $\sigma_{\theta,p}$ for the narrowest offshore spectra. While model hindcasts that account for the broadening effect of wave–bottom Bragg scattering generally agree well with the observed $\sigma_{\theta,p}$ variations, the predicted values still tend to be biased low near the shore, suggesting that there may be other unknown processes that broaden the wave spectrum across the shelf.

Acknowledgments. This research is supported by the Coastal Dynamics Program of the U. S. Office of Naval Research, the French Navy Hydrographic and Oceanographic Service, and the U.S. National Science Foundation (Grant OCE-0114875). Buoys X1 through X6 were deployed and maintained by staff from the Naval Postgraduate School and the Scripps Institution of Oceanography Center for Coastal Studies. We thank the crew of R/V *Cape Hatteras* for excellent support. Wave data from the 8-m-depth array and waverider buoy WR were provided by the Field Research Facility of the U.S. Army Engineer Waterways Experiment Station's Coastal Engineering Research Center, and data from buoy 44014 and C-MAN stations DSLN7 and CHLV2 were provided by the National Data Buoy Center (available online at http://www.ndbc.noaa.gov). Permission to use these data is appreciated. Both R. E. Jensen and C. Long generously helped us with the analysis of these data, and W. Birkemeier and the FRF staff provided flawless logistics support during SHOWEX. Bathymetric data was obtained from the U. S. National Oceanographic Data Center. F. Dobson, M. Donelan, and T. P. Stanton organized and collected the high-resolution multibeam bathymetry data onboard the Canadian Garde Côtière vessel *F. G. Creed.* We note that M. Orzech contributed significantly to the synthesis of the bathymetry dataset. Fruitful comments and encouragement from T. P. Stanton, E. B. Thornton, R. E. Jensen, M. Donelan, and K. Belibassakis are gratefully acknowledged.

REFERENCES

Ardhuin, F., and T. H. C. Herbers, 2002: Bragg scattering of random surface gravity waves by irregular sea bed topography. *J. Fluid Mech.,* **451,** 1–33.

——, ——, and W. C. O'Reilly, 2001: A hybrid Eulerian–Lagrangian model for spectral wave evolution with application to bottom friction on the continental shelf. *J. Phys. Oceanogr.,* **31,** 1498–1516.
——, T. G. Drake, and T. H. C. Herbers, 2002a: Observations of wave-generated vortex ripples on the North Carolina continental shelf. *J. Geophys. Res.,* **107,** 3143, doi:10.1029/2001JC000986.
——, W. C. O'Reilly, T. H. C. Herbers, and P. F. Jessen, 2002b: Spectral evolution of swell across the continental shelf. *Proc. Fourth Int. Symp. on Ocean Wave Measurement and Analysis,* San Francisco, CA, ASCE.
——, ——, ——, and ——, 2003: Swell transformation across the continental shelf. Part II: Validation of a spectral energy balance equation. *J. Phys. Oceanogr.,* **33,** 1940–1953.
Bouws, E., and G. J. Komen, 1983: On the balance between growth and dissipation in an extreme depth-limited wind-sea in the southern North Sea. *J. Phys. Oceanogr.,* **13,** 1653–1658.
Graber, H. C., and O. S. Madsen, 1988: A finite-depth wind–wave model. Part I: Model description. *J. Phys. Oceanogr.,* **18,** 1465–1483.
Grant, W. D., and O. S. Madsen, 1979: Combined wave and current interaction with a rough bottom. *J. Geophys. Res.,* **84,** 1797–1808.
Green, M. O., 1986: Side-scan sonar mosaic of a sand ridge field: Southern Mid-Atlantic Bight. *Geo-Mar. Lett.,* **6,** 35–40.
Hasselmann, K., 1966: Feynman diagrams and interaction rules of wave–wave scattering processes. *Rev. Geophys.,* **4,** 1–32.
——, and Coauthors, 1973: Measurements of wind-wave growth and swell decay during the Joint North Sea Wave Project. *Dtsch. Hydrogr. Z.,* **8** (12) (Suppl. A), 1–95.
Herbers, T. H. C., E. J. Hendrickson, and W. C. O'Reilly, 2000: Propagation of swell across a wide continental shelf. *J. Geophys. Res.,* **105** (C8), 19 729–19 737.
Holthuijsen, L. H., and H. L. Tolman, 1991: Effects of the Gulf Stream on ocean waves. *J. Geophys. Res.,* **96** (C7), 12 755–12 771.
Johnson, H. K., and H. Kofoed-Hansen, 2000: Influence of bottom friction on sea surface roughness and its impact on shallow water wind wave modeling. *J. Phys. Oceanogr.,* **30,** 1743–1756.
Kuik, A. J., G. P. van Vledder, and L. H. Holthuijsen, 1988: A method for the routine analysis of pitch-and-roll buoy wave data. *J. Phys. Oceanogr.,* **18,** 1020–1034.
Li, M. Z., and C. L. Amos, 1999: Sheet flow and large wave ripples under combined waves and currents: Field observations, model predictions and effect on boundary layer dynamics. *Cont. Shelf Res.,* **19,** 637–663.
Long, C. E., and J. Atmadja, 1994: Index and bulk parameters for frequency–direction spectra measured at cerc field research facility, September 1990 to August 1991. Tech. Rep. CERC-94-5, U.S. Army Engineer Waterways Experiment Station, Vicksburg, MS, 245 pp.
Long, R. B., 1973: Scattering of surface waves by an irregular bottom. *J. Geophys. Res.,* **78** (33), 7861–7870.
——, 1980: The statistical evaluation of directional spectrum estimates derived from pitch/roll buoy data. *J. Phys. Oceanogr.,* **10,** 944–952.
Lygre, A., and H. E. Krogstad, 1986: Maximum entropy estimation of the directional distribution in ocean wave spectra. *J. Phys. Oceanogr.,* **16,** 2052–2060.
Madsen, O. S., and W. D. Grant, 1976: Quantitative description of sediment motion by waves. *Proc. 15th Int. Conf. on Coastal Engineering,* vol. II, Honolulu, HI, ASCE, 1093–1112.
——, P. P. Mathisen, and M. M. Rosengaus, 1990: Movable bed friction factors for spectral waves. *Proc. 22d Int. Conf. on Coastal Engineering,* Delft, Netherlands, ASCE, 420–429.
Mathisen, P. P., and O. S. Madsen, 1999: Wave and currents over a fixed rippled bed. 3. Bottom and apparent roughness for spectral waves and currents. *J. Geophys. Res.,* **104** (C8), 18 447–18 461.
Mei, C. C., 1989: *Applied Dynamics of Ocean Surface Waves,* 2d ed. World Scientific, 740 pp.
Munk, W. H., and M. A. Traylor, 1947: Refraction of ocean waves: A process linking underwater topography to beach erosion. *J. Geology,* **LV** (1), 1–26.
Nielsen, P., 1981: Dynamics and geometry of wave-generated ripples. *J. Geophys. Res.,* **86** (C7), 6467–6472.
O'Reilly, W. C., and R. T. Guza, 1993: A comparison of two spectral wave models in the Southern California Bight. *Coastal Eng.,* **19,** 263–282.
Shields, A., 1936: Application of similarity principles and turbulence research to bedload movement. Hydrodynamic Lab. Rep. 167, California Institute of Technology, 43 pp.
Soulsby, R., 1997: *Dynamics of Marine Sands, a Manual for Practical Applications.* Thomas Telford Publications, 256 pp.
Tolman, H. L., 1994: Wind waves and moveable-bed bottom friction. *J. Phys. Oceanogr.,* **24,** 994–1009.
——, 1995: Subgrid modeling of moveable-bed bottom friction in wind wave models. *Coastal Eng.,* **26,** 57–75.
Tournadre, J., 1993: Time and space scales of significant wave heigts. *J. Geophys. Res.,* **98** (C3), 4727–4738.
Traykovski, P., A. E. Hay, J. D. Irish, and J. F. Lynch, 1999: Geometry, migration, and evolution of wave orbital ripples at LEO-15. *J. Geophys. Res.,* **104** (C1), 1505–1524.
Wallbridge, S., G. Voulgaris, B. N. Tomlison, and M. B. Collins, 1999: Initial motion and pivoting characteristics of sand particles in uniform and heterogeneous beds: Experiment and modelling. *Sedimentology,* **46,** 17–32.
Weber, S. L., 1988: The energy balance of finite depth gravity waves. *J. Geophys. Res.,* **93,** 3601–3607.
Wilson, K. C., 1989: Friction of wave-induced sheet flow. *Coastal Eng.,* **12,** 371–379.
Young, I. R., and R. M. Gorman, 1995: Measurements of the evolution of ocean wave spectra due to bottom friction. *J. Geophys. Res.,* **100** (C6), 10 987–11 004.
Zhukovets, A. M., 1963: The influence of bottom roughness on wave motion in a shallow body of water. *Izv. Akad. Nauk SSSR, Seriya Geofizicheskaya,* **10,** 1561–1570.